

Examination of permittivity for depolarization field of ferroelectric by ab initio calculation, suggesting hidden mechanisms

Watanabe, Yukio
Kyushu University

<https://hdl.handle.net/2324/4354936>

出版情報 : Scientific reports. 11 (2155), pp.1-, 2021-01-25. Springer Nature
バージョン :
権利関係 : (C) The Author(s) 2021. This article is licensed under a Creative Commons Attribution 4.0 International License





OPEN

Examination of permittivity for depolarization field of ferroelectric by ab initio calculation, suggesting hidden mechanisms

Yukio Watanabe

Electrostatics of depolarization field E_d in relation to the polarization is studied. In particular, the value of permittivity for E_d (ϵ_d) in prototypical situations of ferroelectrics, including Mehta formula, is examined by ab initio calculations. By using spontaneous polarization P_s corresponding to accurate experiment ones, we show $\epsilon_d = 1$, which suggests that the results of $\epsilon_d \gg 1$ indicate hidden mechanisms; $\epsilon_d = 1$ suggests that the effect of E_d is significant to induce intriguing important phenomena overlooked by $\epsilon_d \gg 1$. A bridge between $\epsilon_d = 1$ and $\epsilon_d \gg 1$, i.e. the consistency of $\epsilon_d = 1$ with conventional results is presented. The exact electrostatic equality of head-to-head–tail-to-tail domains to free-standing ferroelectrics is deduced. Hence, most stoichiometric clean freestanding monodomain ferroelectrics and head-to-head–tail-to-tail domains are shown unstable regardless of size, unless partially metallic. This verifies the previous results in a transparent manner. This conclusion is shown consistent with a recent hyperferroelectric LiBeSb and “freestanding” monolayer ferroelectrics, of which origin is suggested to be adsorbates. In addition, this restriction is suggested to break in externally strained ultrathin ferroelectrics. The macroscopic formulas of E_d are found valid down to a several unit-cells, when electronic and atomic-scale surface effects are unimportant and accurate P_s is used.

Ferroelectrics (FEs) have reversible spontaneous polarization P_s that is useful in various applications, for which high insulativity is desired. Therefore, ideal insulativity of FE is assumed in most studies. In such high insulativity FEs, the depolarization field E_d exists universally even in the absence of external electric field E_{ext} , owing to the charge $-\nabla \cdot P_s$ originating from inhomogeneity or the existence of surface; For a homogeneous P_s , E_d disappears for infinite FE without surface or FE with no surface effect and ideal metal electrodes.

Although analytical formulas of E_d are unnecessary in ab initio calculations, they are indispensable for non ab initio examinations of P_s configurations, stability of domains, and critical thicknesses of FEs^{1–17}. These formulas use the permittivity for E_d (ϵ_d), of which difference affects critically the results. No controversy exists for $\epsilon_d = \epsilon_f$ used in combination with an initial P_s that is an ideal bulk P_s for no macroscopic field in FE as in Kittel models^{1,2}. Here, ϵ_f is static linear permittivity ϵ_r of FE. Otherwise, the choice of ϵ_d is controversial.

Because the polarization P under E_{ext} is $P = P_s + (\epsilon_f - 1)\epsilon_0 E_{ext}$ (ϵ_0 : vacuum permittivity) and the permittivity of FE under E_d is still $\epsilon_f \gg 1$ (“Results”), the standard choice of ϵ_d is ϵ_f ^{4–10,16,17}. We define accurate P_s as P_s obtained by accurate experiments of ideal samples; Accurate P_s can be obtained from ion and electron distribution, e.g. by transmission electron microscopy TEM. When a FE is homogeneous or single-domained, accurate P_s can be obtained by standard electrical measurements (“Results”). An alternate description of accurate P_s is that P_s is a total polarization under the influence of E_d and $E_{ext} = 0$.

Examples of $\epsilon_d = \epsilon_f$ are followings, which are for single domain homogeneous FEs. In this paragraph, “experimental” P_s refers to P_s of each specific sample, which is obtained by the measurements of that sample or is P_s of similar samples. Mehta et al.⁴ studied E_d in capacitors, using experimental $\epsilon_d = \epsilon_f = 1000$ and $P_s = 10 \mu\text{C}/\text{cm}^2$ obtained from the saturated polarization of thin film capacitors. Black et al.⁵ studied E_d of thin film capacitors, using experimental $\epsilon_d = \epsilon_f = 350$ obtained from the polarization-hysteresis near saturation and P_s obtained from the saturated polarization. Zhao et al.⁶ estimated E_d of poly-vinylidene fluoride–trifluoroethylene [P(VDF–TrFE)]

Kyushu University, Fukuoka, Japan. email: watanabe@phys.kyushu-u.ac.jp

thin films by using $E_d = -P_s/\epsilon_f\epsilon_0$ with P_s from remnant polarization measurements ($7 \mu\text{C}/\text{cm}^2$) and $\epsilon_d = \epsilon_f = 10$. In the electrostatic study of Tian et al.⁷, E_d in BiFeO₃ thin films was estimated by using $\epsilon_f = 60$ (in Eq. (1) of Ref.⁷), where this P is initially a total polarization of a single domain state. Kim et al.⁸ estimated E_d in BaTiO₃ (BTO) ultrathin films through the formula by Mehta⁴ with the experimental remnant P obtained from pulse train methods and $\epsilon_d = \epsilon_f = 80$ from $\epsilon_f - E_{\text{ext}}$ curves. In the Ginzburg–Landau–Devonshire (GLD) theory of BTO ultrathin films by Jo et al.⁹, E_d was given through the Mehta formula⁴ with the same P as P in the GLD equation and $\epsilon_d = \epsilon_f = 80$ of Ref.⁸, where P in GLD theory is the total polarization. Schroeder et al.¹⁰ estimated E_d in HfO₂ and PZT ultrathin films through the Mehta formula⁴ with experimental P_s and $\epsilon_d = \epsilon_f = 20$ –300. Similar analyses with $\epsilon_d = \epsilon_f \gg 1$ are frequently employed^{16,17}.

Contrastingly, a primitive considerations show $\epsilon_d = 1$ for P_s , i.e. a total P_s ($\equiv P(E_f(E_{\text{ext}}=0))$)¹³, where E_f is the total macroscopic electric field in FE. For freestanding FEs, for example, $E_f(E_{\text{ext}}) = E_{\text{ext}} - P(E_f(E_{\text{ext}}))/\epsilon_0$ or $E_f(E_{\text{ext}}) = E_{\text{ext}}/\epsilon_f - P(E_f(E_{\text{ext}}=0))/\epsilon_0$ (“Results”). This implies that $\epsilon_d = \epsilon_f$ ^{4–10,16,17} may be double counting, while we note that the electrical measurements of P_s ^{4–10,16,17} are indirect measurements based on induced charge per area in electrodes Q . If $\epsilon_d = 1$ is correct, the successes of the analyses using $\epsilon_d = \epsilon_f$ are attributed to inappropriate parameters or unidentified screening mechanisms.

We think that the existence of this controversy on ϵ_d is due to explanations based on macroscopic quantities. Because macroscopic explanations are abstract, they are unsuitable to bridge the gap between two conflicting views of ϵ_d . On the other hand, ab initio estimation of ϵ_d is considered as the clearest method for this problem but is not reported to our knowledge. Hence, we clarify ϵ_d in the formulas of E_d by ab initio simulations in which ab initio P_s is exactly $P(E_f(E_{\text{ext}}=0))$, which is considered as P_s obtained by accurate experiments of ideal samples. Here, the standard theoretical assumptions: pure, stoichiometric, clean FEs are used.

E_d is related to fundamental issues such as stability of monodomains, critical thicknesses of FE, and the emergence of ferroelectricity in superlattices. Some of these subjects require the consideration of other effects such as strain-induced FE and electronic effect at electrodes¹¹. To avoid the complexity, we concentrate on free-standing insulating FE and its electrostatic identicals, i.e. head-to-head–tail-to-tail (HH–TT) domains. Thus, we estimate the value of ϵ_d in the formula of E_d in a clear manner.

As expected from the electronic interaction at the electrode¹¹, it may be argued that the formula of E_d based on electrostatics is not possible for nm-FEs. We resolve this by focusing on the formulas of E_d and using ab initio P_s in the formulas. Therefore, P_s in these formulas contains the effects of the interactions in slabs or superlattices, whereas the absence of these effects in conventional studies has limited the applicability. The use of nonlinear ϵ_f is often better than linear ϵ_f but can be approximated by an average linear ϵ_f ¹². Therefore, the conclusions below are applicable also to the nonlinear ϵ_f ($\gg 1$).

Model

For simplicity, we discuss 1-dimensional (1D) cases with $E_{\text{ext}} = 0$, where FEs with thickness l_f are in periodic slabs (Fig. 1). Here, 1D refers not to the shape of object (Fig. 2) but to the case where all the properties change only along one coordinate; Fig. 1a,b show FE in vacuum with thickness l_v and FE/paraelectric (I_{adj}) superlattice, respectively, while the latter mimics an inhomogeneous FE. I_{adj} stands for both vacuum and insulator, which is dielectric or FE having different P_s . The polarization, thickness, and permittivity of I_{adj} are P_i , l_i , and ϵ_i , respectively, and the thickness of slab is $l_{\text{SC}} = l_f + l_i$ (l_i). The angles of the polarization P of FE and I_{adj} to the slab direction are θ and θ_i , respectively.

The macroscopic and atomic electrostatic potential (ϕ) of these models are represented by Fig. 1c,d, respectively. ab initio E_d ($E_d^{\text{ab initio}}$) was obtained from the envelope of the peak tops of atomic electrostatic potential, of which example is Fig. 1d. All these FE/vacuum and FE/paraelectric exhibited the density of states (DOS) of insulators (Fig. 1e,f). Additionally, BaTiO₃ (BTO) capacitors are examined, where metal layers are standard electrode materials for FEs: SrRuO₃ or Pt and $\sim 20 \text{ \AA}$ (Fig. 1g).

Accurate estimation of P_s is indispensable for estimating E_d correctly and achieved by direct Berry phase calculations. To enable these calculations, we designed special FE slabs and procedures described in “Methods”. This is because stable 1D-FEs in vacuum are metallic^{14,15} and, hence, direct Berry phase calculations are not possible; Even a two unit-cell thick ($\sim 8 \text{ \AA}$) BTO in vacuum is metallic, when FE is enforced¹⁸. To achieve insulativity, we used tetragonal (P4mm) SrTiO₃ (STO) of which a -axis lattice constant increased by 0.5% and decreased by 0.01% from that of the theoretical cubic phase. For these a -axis lattice constants, bulk STO was FE¹⁹. We refer to them as STO1.005 and STO.9999, respectively, of which bulk P_s ’s were $3.56 \mu\text{C}/\text{cm}^2$ and $6.15 \mu\text{C}/\text{cm}^2$, respectively, by VASP^{19–28}.

Macroscopic equations of E_d are obtained in a following manner. The normal component of P of FE (P_\perp) under E_d is $P_\perp = P_s \cos \theta + (\epsilon_d - 1) \epsilon_0 E_d$ in standard approaches^{4–10,16,17}. The equation of continuity of electric flux is $P_s \cos \theta + \epsilon_d \epsilon_0 E_d = P_i \cos \theta_i + \epsilon_0 E_i$, where E_i is the macroscopic electric field in I_{adj} . The validity of this continuity in the presence of peaks at the surfaces (Fig. 1d) is explained in “Methods”. The continuity of potential in a periodic boundary condition yields $E_i l_i = -E_d l_f$ (Fig. 1c). Therefore, we have for $\theta = 0$

$$E_d = -\frac{P_s - P_i}{\epsilon_0 \left(\epsilon_d + \frac{l_f}{l_i} \right)}. \quad (1)$$

For $\theta \neq 0$ and $\theta_i \neq 0$, Eq. (1) is $E_d = -(P_s \cos \theta - P_i \cos \theta_i)/\epsilon_0(\epsilon_d + l_f/l_i)$. In the present study, P_s and P_i in Eq. (1) are given by ab initio calculations that simultaneously yield E_d consistent with P_s . Therefore, the only unknown quantity is ϵ_d .

When $P_i = (\epsilon_i - 1) \epsilon_0 E_i$, Eq. (2) for $\theta = 0$ is

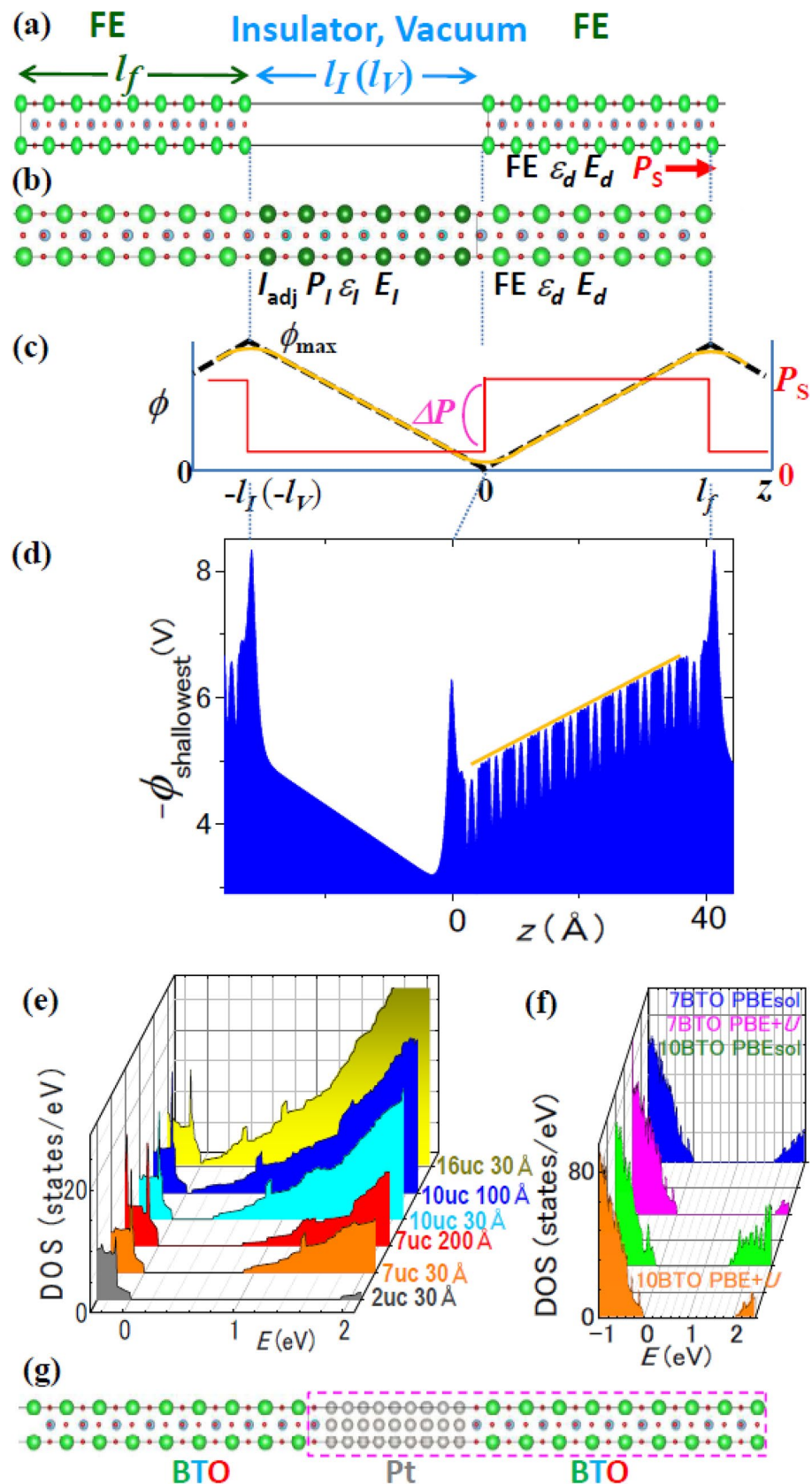


Figure 1. Atomic model of (a) FE/vacuum and (b) FE/I_{adj} where FE is BTO and I_{adj} is STO. BTO/STO serves also as a mimic of an inhomogeneous FE. (c) Macroscopic model. The minimum and maximum electrostatic potential ϕ are 0 and ϕ_{max} , respectively. (d) Example of estimation of E_d from the atomic $-\epsilon\phi$. The orange line shows the envelope yielding E_d . (e) Progressive development of 2D metallic layer: DOS of STO1.005/vacuum, where l_f in unit-cells and l_I in Å are shown on the right. 10-unit-cell-STO with $l_V = 100$ Å is marginally insulating, while 16-unit-cell-STO with $l_V = 30$ Å is metallic. The insulating slabs are used in Fig. 3. P_s in the slab was typically $1 \mu\text{C}/\text{cm}^2$. (f) DOS of 7 and 10-unit-cell BTO/5-unit-cell-STO calculated with PBEsol and PBE + U. (g) Atomic model of BTO/Pt.

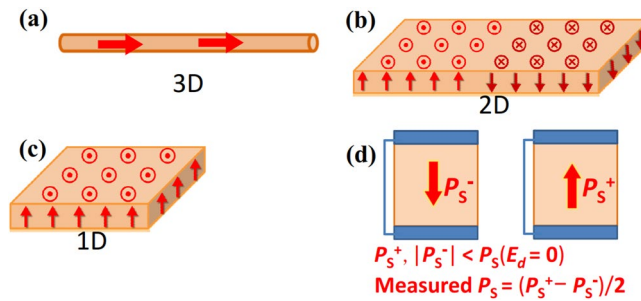


Figure 2. Definition of (a) three, (b) two, (c) one-dimensions for FE in this article. Dimensionality is not referred to the shape of an object. θ is the angle between the normal to the surface in (c) and the direction of P_s . (d) Typical measurement of P_s in a capacitor. This is smaller than bulk P_s ($E_d = 0$), because of nonzero screening length in electrodes.

$$E_d = -\frac{P_s}{\epsilon_0 \left(\epsilon_d + \frac{\epsilon_l l_f}{l_f} \right)}. \quad (2)$$

For $\theta \neq 0$ and $\theta_f \neq 0$, Eq. (2) is $E_d = -P_s \cos \theta / \epsilon_0 (\epsilon_d + \epsilon_l l_f / l_f)$.

Equation (2) yields also E_d in FE capacitors, because equations of continuity of electric flux similar to the above hold; A short-circuited FE capacitor is modelled as a perfect-metal/insulator($l_f/2$)/FE/insulator($l_f/2$)/perfect-metal²⁹, where the perfect metal refers to a metal with zero screening length and the thickness of each screening layer λ is $l_f/2$. Assuming $P_1 = \epsilon_f \epsilon_0 E_f$ in screening layer, Eq. (2) is applicable and yields the Mehta formula⁴ with $\epsilon_d = \epsilon_f$ and $l_f = 2\lambda$. For FE capacitors with $\theta \neq 0$, the formula beneath Eq. (2) is applicable. Because we neglected the electronic interactions at the metal/FE interface of 1–2 unit-cell, e.g. quantum mechanical smearing³⁰, the formula for capacitors may be inaccurate for $l_f <$ several unit-cells.

The nominal FE thickness l_f is the distance between the center position of a top ion and that of a bottom ion, but twice of the atom radius $\sim 0.5 \text{ \AA} \times 2$ should be added. In case of FE/vacuum, this correction was examined by considering the smear-out of electrons into vacuum²⁹; When λ_{smear} ($\sim 0.8 \text{ \AA}$) is the distance between an outermost electron density and a center of ion position (“Methods”), FE thickness appropriate for electrostatics is $l_f^{\text{eff}} = l_f + 2\lambda_{\text{smear}}$. As seen below, Eqs. (1) and (2) can be valid down to a few nm l_f in case of FE/vacuum. Additionally, surface buckling layer is electrostatically a dipole layer, and its net charge is zero. Therefore, even in the presence of buckling layer, these formulas for 1D are also valid, by regarding buckling layer as dead layer (“Methods”); The effective thickness is $l_f^{\text{eff}} - 2l_{\text{buckle}}$, where l_{buckle} is the thickness of a buckling layer ~ 1 –2 unit-cells.

Results

Estimation of ϵ_d . ϵ_d was examined through the comparison of ab initio E_d with E_d of Eq. (1) or (2) that uses different values of ϵ_d . For FE/vacuum ($P_f = 0$), P_s in Eq. (1) was the rigorously calculated P_s of the slab by Berry phase. For FE/insulators and FE capacitors, P_s and P_f in Eq. (2) were calculated ab initio. Therefore, all the parameters in Eqs. (1) and (2) except for ϵ_d are accurately known.

Figure 3 compares E_d 's by Eq. (1) with $E_d^{\text{ab initio}}$'s, where Eq. (1) uses $\epsilon_d = 1, 4$. Here, $\epsilon_d = 4$ is the lower bound of electronic permittivity of STO²⁹. $E_d^{\text{ab initio}}$ is accurate for a long l_f and data for $l_f \gg l_f$ reflects the effect of ϵ_d explicitly because of $E_d \sim -P_s / \epsilon_0 \epsilon_d$. Large symbols in Fig. 3 show the data points satisfying both conditions and, hence, are important.

In Fig. 3, Eq. (1) with $\epsilon_d = 1$ agrees with $E_d^{\text{ab initio}}$ within 10% always for $\lambda_{\text{smear}} = 0.8 \text{ \AA}$ and mostly for $\lambda_{\text{smear}} = c/2$. The difference between E_d 's for $\lambda_{\text{smear}} = 0.8 \text{ \AA}$ and $c/2$ provides typical error bar and is approximately 10%. Equation (1) with $\epsilon_d = 4$ deviates from $E_d^{\text{ab initio}}$'s by more than 140%, and the deviations increase monotonically with ϵ_d . Additionally, Eq. (1) yields the potential difference $\phi_{\text{max}} = |E_d| l_f = P_s / \epsilon_0 (\epsilon_d l_f + 1/l_f)$, which, with $\epsilon_d = 1$, quantitatively agrees with bandgap E_g that decreases with l_f and l_f in Fig. 1e.

For BTO/STO, Fig. 4 compares E_d 's by Eq. (1) with $E_d^{\text{ab initio}}$'s, where Eq. (1) uses ab initio P_s and ab initio P_f . For $\epsilon_d = 1$, Eq. (1) agrees within $\pm 20\%$ with $E_d^{\text{ab initio}}$. In particular, the agreements are within $\pm 6\%$ in the results by PBE + U (a method of ab initio calculation (“Methods”)). Equation (2) with $\epsilon_d = 20$ deviated by more than 1000% from $E_d^{\text{ab initio}}$. The deviation increased monotonically with ϵ_d , whereas $\epsilon_f > 20$ is usual for inorganic FEs^{4,5,7–10,16,17}.

For capacitors, Fig. 5a,b compare E_d by Eq. (2) with $E_d^{\text{ab initio}}$, where Eq. (2) uses ab initio P_s and $l_f/2\epsilon_f \approx 0.1 \text{ \AA}$, 0.05 \AA ; E_d 's by Eq. (2) with $\epsilon_d = 1$ agrees best with $E_d^{\text{ab initio}}$'s. The disagreements of Eq. (2) with $E_d^{\text{ab initio}}$'s increases with ϵ_d . The differences between open and filled symbols provide typical error bar and are 10–20%. Consequently, all the studied cases indicate $\epsilon_d = 1$ (Figs. 3, 4, 5).

Bridge between $\epsilon_d = 1$ and ϵ_f ¹³. We showed $\epsilon_d = 1$ and will use it below. By noting that electrical measurements of P_s are based on the change of charge per area in electrodes ΔQ induced by E_{ext} , a bridge between $\epsilon_d = 1$ and $\epsilon_d = \epsilon_f$ will be shown. Because most studies^{4–10,16,17} are for FE capacitors, the followings are for 1D FE capacitors with $\theta = 0$, which can represent FE/vacuum for $\epsilon_f = 1$ and freestanding FE for $l_f/\epsilon_f \gg l_f$.

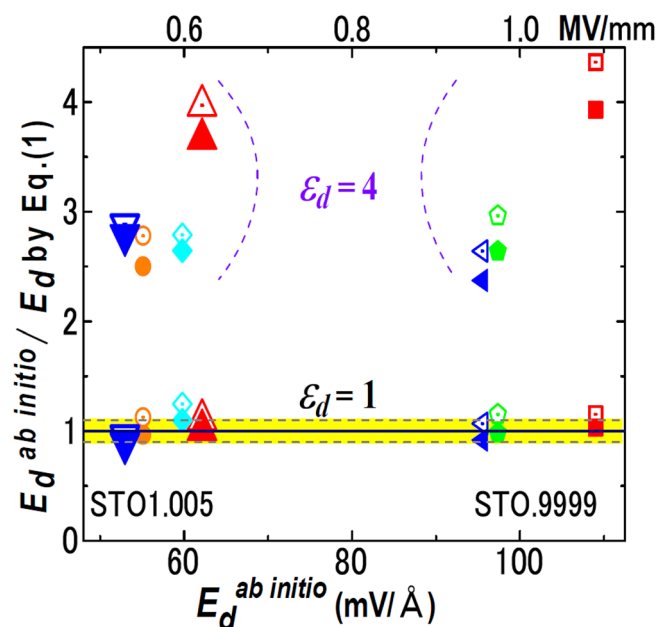


Figure 3. FE/vacuum. Comparison of $E_d^{ab initio}$ with Eq. (1) with $\epsilon_d = 1, 4$ for STO1.005/vacuum and STO0.9999/vacuum. The yellow band shows the range of 1 ± 0.1 . The filled and open symbols represent data in which l_f in Eq. (2) is estimated with $\lambda_{smear} = 0.8 \text{ \AA}$ and $\lambda_{smear} = c/2$, respectively. The shape of symbol indicates a slab structure: For STO1.005, orange circles, red triangles, light blue diamonds, and blue inverted triangles correspond to 7-unit-cell-STO with $l_v = 30 \text{ \AA}$, 7-unit-cell-STO with $l_v = 200 \text{ \AA}$, 10-unit-cell-STO with $l_v = 30 \text{ \AA}$, and 10-unit-cell-STO with $l_v = 100 \text{ \AA}$, respectively. For STO0.9999, red squares, green pentagons, and blue 90° -rotated triangles correspond to 5-unit-cell-STO with $l_v = 300 \text{ \AA}$, 6-unit-cell-STO with $l_v = 30 \text{ \AA}$, and 7-unit-cell-STO with $l_v = 30 \text{ \AA}$, respectively.

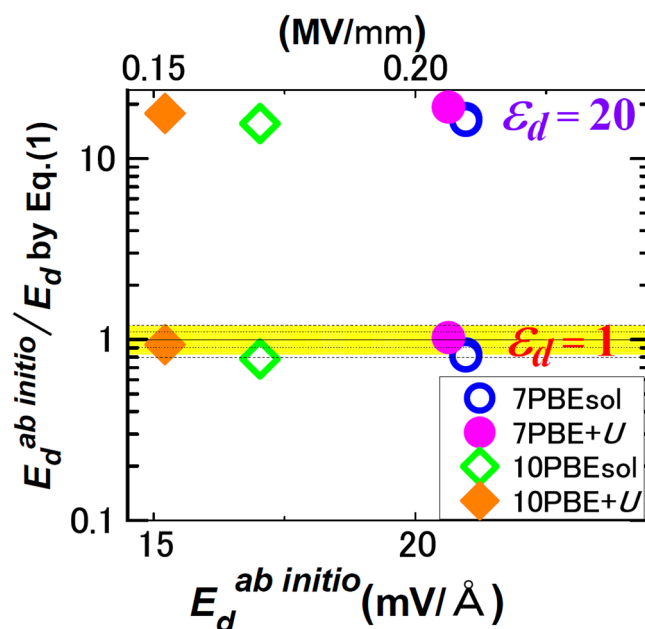


Figure 4. FE/paraelectric. Comparison of $E_d^{ab initio}$ with Eq. (1) with $\epsilon_d = 1, 20$ for BTO/5-unit-cell-STO. The yellow band shows the range of 1 ± 0.2 , and the dotted lines inside of the band show the range of 1 ± 0.1 . Inset explains the BTO thickness l_f in unit-cells and ab initio method (PBEsol or PBE + U).

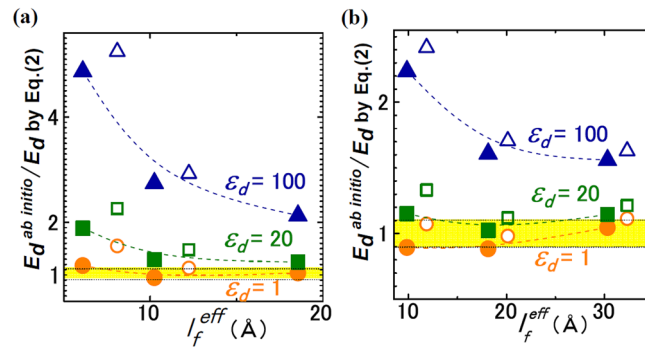


Figure 5. FE capacitor. Comparison of $E_d^{ab initio}$ with Eq. (2) with $\varepsilon_d = 1$ (orange), 20 (green), and 100 (blue) for (a) BTO/SrRuO₃ and (b) BTO/Pt. The filled and open symbols represent the data for $l_f^{eff} = l_{T-B} - uc_{BTO}$, $l_{T-B} = 1.5uc_{BTO}$, respectively.

Using the total electric field in FE E_f and the total polarization of FE P , $P_S \equiv P(E_f(E_{ext}=0))$ and $E_d \equiv E_f(E_{ext}=0)$. When the potential difference between the electrodes is V , Eq. (2) changes to $E_f(V) = V/(l_f + l_f/\varepsilon_f) - P(E_f(E_{ext})) / \varepsilon_0(1 + \varepsilon_f l_f/l_f)$ ¹³. E_f , the field in the screening layer of the electrode, is $E_f(V) = V/\varepsilon_f(l_f + l_f/\varepsilon_f) + P(E_f(E_{ext}))l_f/\varepsilon_0 l_f(1 + \varepsilon_f l_f/l_f)$.

$E_f(V)$ can be written as $E_f(E_{ext}) = E_{ext} + E_d(E_f(E_{ext}))$, where $E_{ext} \equiv V/(l_f + l_f/\varepsilon_f)$ ($= V/l_f$ for $l_f \gg l_f/\varepsilon_f$) and $E_d(E_f(E_{ext})) \equiv -P(E_f(E_{ext}))/\varepsilon_0(1 + \varepsilon_f l_f/l_f)$ similar to Eq. (2).

ε_f is defined by $\varepsilon_f - 1 = \{P(E_f(E_{ext})) - P_S\}/\varepsilon_0(E_f(E_{ext}) - E_d)$, where $E_d = E_f(E_{ext}=0) = -P_S/\varepsilon_0$ for $l_f \gg l_f/\varepsilon_f$, and $\varepsilon_f (\gg 1)$ is linear for $|E_{ext}| \ll |P_S|/\varepsilon_0$. Hence, $P(E_f(E_{ext})) = P_S + (\varepsilon_f - 1)(\varepsilon_0 E_f(E_{ext}) + P_S)$ for $l_f \gg l_f/\varepsilon_f$.

The substitution of this $P(E_f(E_{ext}))$ in the expression of $E_f(E_{ext})$ yields $E_f(E_{ext}) = E_{ext}/\varepsilon_f - P_S/\varepsilon_0$ for $l_f/l_f \gg l_f$ (free-standing), suggesting that the measured permittivity is ε_f .

We show an example: $\Delta Q = \varepsilon_f \varepsilon_0 (E_f(V) - E_f(V=0)) = V/(l_f/\varepsilon_f \varepsilon_0 + l_f/\varepsilon_f \varepsilon_0)$ ¹³ from the above expression of $E_f(V)$. This is equal to $\Delta Q = CV$, where $C = (C_f^{-1} + C_l^{-1})^{-1}$ ($C_f \equiv \varepsilon_f \varepsilon_0/l_f$, $C_l \equiv \varepsilon_f \varepsilon_0/l_f$) is a series capacitance per area. In particular, for $l_f \gg \varepsilon_f l_f/\varepsilon_f$, $\Delta Q = \varepsilon_f \varepsilon_0 V/l_f = C_f V$. Therefore, the permittivity of FE under $E_d = E_f(E_{ext}=0) = -P_S/\varepsilon_0$ is ε_f .

Additionally, Eq. (2) with $\varepsilon_d = 1$ shows $D = P_S - P_S/(1 + \varepsilon_f l_f/l_f)$, while $D = Q$. Because $l_f/\varepsilon_f \sim 0.1$ Å, the difference between the real P_S and the measured P_S is detectable only for $l_f < 10$ Å. As for potential difference, Eq. (2) is well approximated by $E_d = -P_S l_f/(\varepsilon_f \varepsilon_0 l_f)$ for $l_f > 10$ Å, because l_f/ε_f is short ~ 0.1 Å. Therefore, the potential difference across the capacitor is independent of the FE thickness l_f , when the quality of FE is independent of l_f and FE is ideally stoichiometric.

Discussions

Here, we discuss only monodomain FE (Fig. 2c).

Permittivity for non-polarization field (built-in field). Because the polarization P in standard GLD theories^{9,31–34} are formulated with a single *total polarization*, $\varepsilon_d = 1$ should be used in standard GLD theories.

The preceding results have shown that the permittivity that expresses the change of P in response to E_{ext} is $\varepsilon_f (\gg 1)$ even for FE under E_d . By the same logic, the change of P by built-in internal field E^{bi} is also expressed by $\varepsilon_f (\gg 1)$, where E^{bi} is not due to P or a dipole that is not expressed by P . E^{bi} exists in FEs by various mechanisms such as the diffusion potentials at *pn* and Schottky junctions and chemical orders, e.g. LaAlO₃ in the polar catastrophe model.

For example, $P_S = 0$ and $E_d = 0$ in a bulk cubic BTO. However, $E^{bi} \neq 0$, when the surfaces of a cubic BTO slab are asymmetrically terminated to form a dipole, e.g., BaO/TiO₂/BaO/.../TiO₂/BaO/TiO₂. Hence, to achieve $E^{bi} = 0$, the present study used chemically symmetric slabs (Fig. 1a,b,g), e.g. BaO/TiO₂/BaO/.../TiO₂/BaO.

Insulativity condition. For 1D-FE to remain insulating without artifactual screening, $e l_f |E_d| < E_g$ (e : elementary charge), for which Eq. (2) and $\varepsilon_d = 1$ yield $1/l_f > e P_S \cos \theta / \varepsilon_0 E_g - \varepsilon_f/l_f$. Therefore, the condition of insulativity is one of the followings

$$l_f \leq 1.8 \text{ Å} \varepsilon_f \frac{E_g^*}{P_S^*(T_C) \cos \theta}, \quad (3)$$

$$l_f < 1.8 \text{ Å} \left(\frac{P_S^*(T_C) \cos \theta}{E_g^*} - 1.8 \text{ Å} \frac{\varepsilon_f}{l_f} \right)^{-1}, \quad (4)$$

where E_g^* and $P_S^*(T_C)$ are bulk E_g normalized by 2 eV and P_S of bulk FE at T_C normalized by 10 $\mu\text{C}/\text{cm}^2$, respectively, and the unit of l_f and l_v is Å. P_S of bulk FE at T_C approximates the critical P_S of FE that is about to become paraelectric by E_d ¹². Equations (3) and (4) explain the insulativity of FEs in Fig. 1e,f.

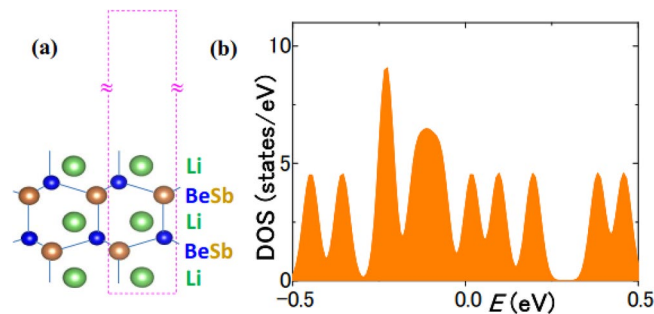


Figure 6. (a) Atomic model of LiBeSb/vacuum. (b) DOS showing metallicity of LiBeSb/vacuum.

Freestanding insulating FE and HH-TT. The giant permittivity and large piezoelectric coefficients of FE are regarded as an *electrical softness* due to the tailing-effect of structural instabilities, i.e. phase transitions. This suggests that these properties are incompatible with an extremely stable FEs. For freestanding FEs ($l_f = \infty$, $\theta = 0$), Eq. (3) yields $l_f < 1.8 \text{ \AA} (E_g/2 \text{ eV}) / (P_s(T_C)/10 \text{ \mu C/cm}^2)$. This suggests that freestanding FEs with normal bulk properties are FEs with metallic layer or insulating paraelectrics^{12,15} as explained by the following GLD analysis. This conclusion is valid also for HH-TT domains with $\theta = 0$.

Standard GLD theories are based on a single polarization vector P as the order parameter. We approximate the polarization possibly missed in such GLD theory²⁹ by an extra permittivity $\epsilon_{NG} - 1$ ^{35,36}, while ϵ_{NG} is speculatively close to electronic permittivity²⁹. The GLD energy F of an *insulating* FE is $F = (T - T_0)P^2/2C\epsilon_0 + \beta P^4/4 + \gamma P^6/4 - PE_d/2$, where T_0 , C , β , γ , and θ are Curie-Weiss temperature, Curie constant, and GLD coefficients, respectively. The effect of strain can be incorporated in T_0 and β ^{31-34,37}. Curie temperature T_C is $T_0 + \Delta T$, where $\Delta T = 3\beta^2/16\gamma C\epsilon_0$. For 2nd order transition, $\gamma = 0$, $\beta > 0$, and $T_C = T_0$. The effect of $E_d = -P_s/\epsilon_0\epsilon_{NG}$ is the change of T_0 to $T_0 - C/\epsilon_{NG}$ in F , where Eq. (2) with $\epsilon_d = \epsilon_{NG}$ and $l_f = \infty$ is used.

Hence, the existence of freestanding FE that undergoes 2nd order FE transition is $T_C > C/\epsilon_{NG}$. This means $\chi_{GL} < \epsilon_{NG}/2$ at $T = 0$, because $\chi_{GL} = C/2T_C$ at $T = 0$. The total permittivity $\epsilon_f = \chi_{GL} + \epsilon_{NG}$ at $T = 0$ is $< 3\epsilon_{NG}/2$ and < 7.5 for $\epsilon_{NG} = 5$ ²⁹.

Similarly, for FE undergoing 1st order FE transition, it is known that $\chi_{GL} = 1/\{(T - T_0)/C\epsilon_0 + 3\beta P^2 + 5\gamma P^4\}$ at $T < T_C$. Stable state satisfies $\partial F/\partial P = (T - T_0)/C\epsilon_0 + \beta P^2 + \gamma P^4 = 0$. Therefore, $\chi_{GL} = 1/(4T_0/C\epsilon_0 - 2\beta P^2)\epsilon_0 < C/4T_0$ at $T = 0$ (We assume $T_0 > 0$), and $T_C = T_0 + \Delta T = T_0 + 3\beta^2/16\gamma C\epsilon_0$. Because $\Delta T \ll T_0$ in almost all FEs^{2,31-34}, we may assume $T_C < 2T_0$. Under this assumption, $\chi_{GL} < C/2T_C$ at $T = 0$, and $C < \epsilon_{NG}T_C$ means $\chi_{GL} < \epsilon_{NG}/2$ at $T = 0$. $\epsilon_f = \chi_{GL} + \epsilon_{NG} < 3\epsilon_{NG}/2$ at $T = 0$, which is < 7.5 for $\epsilon_{NG} = 5$.

These ϵ_f 's of FEs undergoing 2nd and 1st transitions appear too small for experimentally observed bulk metal oxide FEs. Therefore, freestanding insulating FEs satisfying $C < \epsilon_{NG}T_C$ are unlikely to exist, unless ϵ_{NG} is far larger than 5; That is, for freestanding FE materials, there exists virtually one choice between a partial loss of insulativity and a loss of FE.

Design of freestanding insulating FE. For freestanding insulating FE ($\theta = 0$), $C < \epsilon_{NG}T_C$ was shown, while $\Delta\phi \sim P_s(E_d)l_f/\epsilon_0$. Therefore, FE materials having a very large $\epsilon_{NG} (\gg 5)$ can retain FE and remain insulating, when ultrathin. Such FE materials are unlikely to exist. Alternatively, we may consider *electrically freestanding* FE or FE with clean surface that is not mechanically freestanding. In this case, T_0 ($\sim T_C$) of common FEs increases to T_0^{eff} by inplane strain, while ab initio calculations shows that T_0^{eff} is much larger than those of standard GLD theories³⁷. Therefore, heavily strained FE materials may retain FE and remain insulating, when ultrathin (Formula estimating an effective T_0 from ab initio P_s is Ref. [88] of Ref. [37]). The above indicates that ϵ_f of such FE is extremely low for $E_d = 0$ but can be large for $E_d \neq 0$, because the coefficient of the first term GLD energy F is $(T - T_0^{eff} + C/\epsilon_{NG})/2C\epsilon_0$ (freestanding).

LiBeSb. LiBeSb with $P6_3mc$ symmetry³⁸ is reported as a hyper-FE that retains both FE and insulativity in FE/paraelectric superlattices, which may contradict the above conclusion on insulativity and FE stability. Therefore, we ab initio calculated one-unit-cell LiBeSb ($l_f = 6.08 \text{ \AA}$) in vacuum (Fig. 6a). Figure 6b shows a metallic DOS of LiBeSb for $l_v = 31.7 \text{ \AA}$, while metallicity increases with l_v . This is consistent with the above conclusion and the previous reports^{14,15,39-41}. Equations (3) and (4) explain the insulativity of LiBeSb³⁸ as the effect of adjacent dielectric. Actually, similar to LiBeSb, BTO/STO superlattices are insulating as in Fig. 1f, while BTO/vacuum is partially metallic¹⁸.

Freestanding and free-surface FE: hidden mechanism. Mechanically freestanding FE is customarily referred to as freestanding; Ji et al.⁴² reported exceptionally intriguing results of the freestanding insulating BiFeO₃ (BFO) that retains FE down to monolayer. This appears to contradict both the reports of metallicity at HH-TT domains of BFO and the present results, esp. the single choice between insulating paraelectric and partially metallic FE.

If $\epsilon_d = \epsilon_f = 100$, the potential difference $\Delta\phi$ across freestanding insulating BFO of 1–4 unit-cell thickness with a moderate $P_s \sim 20 \text{ \mu C/cm}^2$ is 0.09–0.36 V by Eq. (2) with $l_f = \infty$, which allows this BFO to be insulating in agreement with Ji et al.⁴². For $\epsilon_d = 1$, $\Delta\phi$ increases by 100 times, by which BFO's have to be partially metallic.

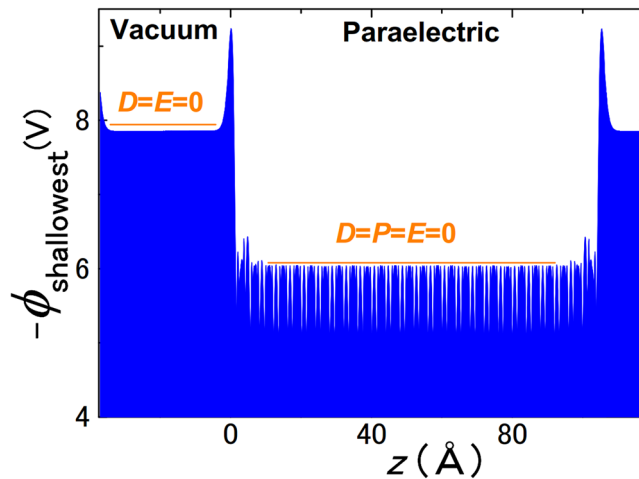


Figure 7. Ab initio electrostatic potential ϕ of paraelectric insulating BTO in vacuum showing peaks due to surface dipoles formed by electron smear-out and buckling. In this calculation of 26.5 unit-cell-BTO slab, all the ion positions are fully relaxed, and the insulating paraelectric state is the lowest energy state. $\phi=0$ in FE means $E_d=0$, for which Eq. (2) suggests $P_s=0$. $P_s=0$ is also directly confirmed by ab initio calculations. Similarly, $E_d=0$ in vacuum. Therefore, $D=0$ in FE and vacuum.

Hence, we shall look at the measurements of Ji et al.⁴² For freestanding FE, it was shown that the surface or boundary of 1–2 unit-cell thickness was metal and the rest was insulating FE^{14,15,39,40}. So, the metallicity is detectable only by inplane conductance, which is absent in Ji et al.⁴². Second, because the crystallographic properties of FE with these metal layers was shown to be those of FE^{14,15,39,40}, the crystallographic measurements of Ji et al.⁴² do not exclude metallic layers. Third, because piezoelectric measurements use bottom and top electrode (or tip) and may move ions⁴³, those by Ji et al.⁴² are not that of freestanding FE. Consequently, all the measurements of Ji et al.⁴² do not contradict the conclusion of the present paper.

More importantly, the interdisciplinarity of nano FE hides true mechanisms. In the present case, “freestanding” is defined by surface science and electrostatics. For example, Fong et al. found monodomain FE of 3 unit-cell thickness as opposed to E_d -limited domain and size effect, which was later attributed to adsorbates⁴⁴. This agrees with recent ab initio study⁴⁵. Further, photoemission spectroscopy in UHV showed that SrTiO₃ surface was covered by adsorbates even in ultrahigh vacuum (UHV)⁴⁶. Actually, the free surface with $P_s \perp$ surface is insulator-like in air and metallic in UHV when cleaned¹⁴. Because the insulating freestanding FE⁴² was exposed to air and water, we suggest adsorbates as its hidden mechanism.

Conclusion

We studied the electrostatics of E_d , especially, the value of permittivity ϵ_d in the formula of E_d by ab initio simulations, where ab initio P_s corresponded accurately to experimental P_s . For this, the standard theoretical assumptions: pure, insulating, stoichiometric, and clean FEs were used. To validate the analyses of E_d based on electrostatics, we concentrated on the formulas of E_d for accurate ab initio total $P(E_f(E_{ext}=0))$ that contained various atomic effects and corresponded to experimental P_s . Further, we focused on the simplest cases of E_d : freestanding 1D-FE, HH-TT domains, and superlattices that mimicked inhomogeneous FE and FE/dielectric.

The present ab initio simulations showed $\epsilon_d = 1 \pm 0.06 - 1 \pm 0.2$. That is, $\epsilon_d = 1$ should be applied to experimental and standard-GLD P_s 's. A contradiction between $\epsilon_d = 1$ and $\epsilon_d = \epsilon_f$ was resolved by a bridge; Even under E_d , the permittivity for E_{ext} and built-in field E^{bi} was ϵ_f . Therefore, if a study requires $\epsilon_d \gg 1$ ^{4–10,16,17}, the value of P_s is incorrect, the values of the parameters are inappropriate, or, most likely, hidden screening mechanisms exist^{14,15,43–48}.

For freestanding insulating FEs ($l_f = \infty$), Eq. (2) yields $E_d = -P_s/\epsilon_0$ (or $E_d = -P_s \cos \theta/\epsilon_0$), while, for HH-TT insulating domains, Eq. (1) with $P_f = -P_s$ and $l_f = l_f$ yields the same E_d . Therefore, when the effects at surface of 1–2 unit-cell is unimportant, freestanding FEs are electrostatically exactly identical with HH-TT domains.

Consequently, both the electrostatic energy of E_d and the FE free energy of insulating freestanding and HH-TT FEs scale linearly with l_f . This implies that the stability of 1D-freestanding and HH-TT insulating FEs is independent of size^{12,15}, when the energy increase by surface effect and domain walls energy is ignored. A strain effect to overcome this restriction was suggested.

Because $l_f P_s/\epsilon_0 < Eg/e$ by $\epsilon_d = 1$, the insulativity required an extremely small bulk $P_s \ll 1 \mu\text{C}/\text{cm}^2$ or paraelectricity (Fig. 7). Alternatively, the stability of 1D-freestanding and HH-TT FEs for $\theta \approx 0$ required a partially metallic FE. This conclusion verified the previous results^{14–16,39–41} in a material-independent manner and was confirmed also for hyper-FE LiBeSb that was reported to be insulating in FE/paraelectric³⁸. This conclusion appeared inconsistent with “freestanding” monolayer BFO⁴². But, the examinations of experimental procedures^{43–46} suggested adsorbates as a hidden mechanism.

The electrostatic formulas of E_d (Eqs. 1 and 2) were valid down to a several unit-cell scale (Figs. 3, 4, 5), when atomic-scale surface effects, e.g. interactions with electrodes^{11,28} were unimportant. Even with buckling at FE surfaces, these formulas can be valid by regarding buckling layers as dead layer.

Methods

Ab initio calculations. In the examinations of FE/vacuum, the results of SrO-terminated STO slabs are presented, because they have E_g wider than E_g of the TiO_2 -terminated STO slabs (Fig. 1e). To enforce FE, the ion-positions in the STO/vacuum slabs were not optimized, because, otherwise, FE disappears (Fig. 7). Therefore, the STO unit-cells in the slabs retained the ion positions of bulk STO1.005 or STO.9999. These calculations of STO/vacuum were only for the examination of E_d and ϵ_d and do not correspond to standard experiments. P_s of STO1.005 in the slab was typically $1 \mu\text{C}/\text{cm}^2$.

The models of FE/paraelectric are BTO/STO superlattices. All the calculated forces were $< 1 \text{ meV}/\text{\AA}$ after geometry relaxation, and the a -axis lattice constant of STO was expanded by 1.1–1.3%. The bulk STOs that had these a -axis lattice constants were paraelectric¹⁹. The a -lattice constant of BTO/SrRuO₃ and BTO/Pt capacitor was fixed at the theoretical a -axis lattice constant of cubic STO and bulk tetragonal BTO, respectively, and all other ion positions were relaxed (Fig. 1g). The atomic models of BTO/SrRuO₃ are similar to BTO/STO (Fig. 1b). The use of the theoretical a -lattice constant of cubic STO corresponds to the thin films on STO substrates. The surfaces of the BTO and SrRuO₃ were TiO_2 and SrO, respectively, and Pt atoms at the interface aligned with O atoms of TiO_2 plane.

The present study is about the formulas of E_d for given structure parameters. Here, the change of P_s by the interactions in the slabs is included consistently in these formulas by the use of ab initio P_s in these formulas.

The ab initio calculations with VASP^{20–22} used the projector augmented wave method²³ with a Monkhorst–Pack²⁴ mesh of $8 \times 8 \times 2$ for slabs and an energy cutoff of 650 eV. PBEsol functional²⁵ was used, unless otherwise mentioned. Ab initio P_s was calculated through Berry phase²⁶. The results of BTO/STO were reexamined with PBE functional²⁷ with Hubbard U (PBE + U)²⁸, which was used also for BTO/Pt. In the slab calculations, graphic processing units acceleration^{49,50} was used. The supercells were produced by VESTA⁵¹.

Accurate estimation of P_s under E_d . For correct ϵ_d , accurate estimations of a total polarization P_s under E_d are essential. Because we compare Eqs. (1) and (2) using ab initio P_s with E_d for the ion positions same as those of this P_s , the accuracy of P_s for given ion positions matters.

Berry phase calculation of P_s for given ion positions is accurate but only possible for insulators. For example, the present Berry phase calculations yields P_s of bulk BaTiO₃ that agree with experimental P_s within 4%, when experimental ion positions and lattice constants of at 303 K are used³⁷.

Therefore, to obtain accurate P_s , the dipole moment of a whole slab was calculated with Berry phase; We treated these slabs as unit-cells to apply Berry phase calculations directly, unlike conventional approaches. P_s was obtained by dividing the dipole moment by the volume of FE part of the slab. These P_s 's were referred to “rigorously calculated P_s 's of the slab” and obtained for all the FE/vacuum and BTO/STO slabs. Here, STO1.005 and STO.9999 slabs are insulating, allowing accurate Berry phase calculations.

Additionally, P_s of the unit-cell that possessed exactly the same ion positions as those in the slab was calculated with Berry phase and, then corrected with atomic polarization by E_d by the procedures in Ref.²⁹. These P_s 's agree perfectly with “rigorously calculated P_s 's of the slab”, which further confirmed the accuracy of the present P_s 's of FE/vacuum and BTO/STO. These corrected P_s 's²⁹ were used for capacitors. Therefore, in the present study, P_s 's are accurate total P_s 's and self-consistent with E_d . Hence, P_s 's in Figs. 3, 4 and 5 are accurate.

Validity of continuity of electric flux and surface dipoles. Equations (1) and (2) are applicable to the regions much larger than unit-cell. Here, the peaks of 1.5 \AA width at the surface in Fig. 1d may be suspected to invalidate Eqs. (1) and (2). These peaks are due to effective surface dipoles caused by electron tunneling smear-out; Surface electrons smear out in vacuum, making positive charge density inside the surface and negative charge density in vacuum.

The heights and shape of the two peaks from the baseline (yellow line in Fig. 1d) are the same (1.53 V). This means $\sigma^+_{\text{R}} = \sigma^+_{\text{L}}$ and $\sigma^-_{\text{R}} = \sigma^-_{\text{L}}$ as expected from their origin, where σ^+_{R} , σ^-_{R} , σ^+_{L} , and σ^-_{L} are positive and negative charge densities that yield the right and left peak, respectively. Because of the charge neutrality of FE, $\sigma^+_{\text{R}} + \sigma^+_{\text{L}} + \sigma^-_{\text{R}} + \sigma^-_{\text{L}} = 0$, i.e. $\sigma^-_{\text{R}} + \sigma^+_{\text{R}} = 0$. Therefore, the continuity of the electric fluxes D_{FE} in FE and D_{I} in I_{adj} (Fig. 1b) is $D_{\text{FE}} - D_{\text{I}} = \sigma^-_{\text{R}} + \sigma^+_{\text{R}} = 0$, i.e. the continuity of electric flux $D_{\text{FE}} = D_{\text{I}}$, where $D_{\text{FE}} = P_s \cos \theta + \epsilon_d \epsilon_0 E_d$ and $D_{\text{I}} = P_{\text{I}} \cos \theta_{\text{I}} + \epsilon_0 E_{\text{I}}$. A clearer example is shown in Fig. 7, which evidently shows the continuity of electric flux and, hence, validates the use of Eqs. (1) and (2).

Because surface buckling in vacuum is electrostatically dipole due to ion displacements, the arguments exactly the same as the above hold. Therefore, the electric flux of the inside D_{FE} and the outside D_{V} of the buckling layer is continuous ($D_{\text{FE}} = D_{\text{V}}$).

Effective l_f (l_f^{eff}). For FE/vacuum, the effective l_f (l_f^{eff}) was estimated from the planar averaged electron density ρ profiles²⁹. Below, $z=0$ corresponds to the position of bottom ion. Because ρ at $z=-0.8 \text{ \AA}$ was same as the minimum ρ of inner part in all the ρ - z curves, the region of $z=0 \sim -0.8 \text{ \AA}$ was considered as a part of FE ($\lambda_{\text{smear}} = 0.8 \text{ \AA}$), and l_f^{eff} was $l_f + 2\lambda_{\text{smear}}$. In addition, $\lambda_{\text{smear}} = c/2$ (half unit-cell) was also tested, and $l_{\text{V}} = l_{\text{SC}} - l_f^{\text{eff}}$. For BTO/STO, l_f was defined as the distance between the top and bottom Ti ions of BTO (Fig. 1b), and $l_{\text{I}} = l_{\text{SC}} - l_f$.

For FE capacitors, l_f^{eff} was $l_{\text{T-B}} - u_{\text{BTO}}$ (outermost ions are Ti, u_{BTO} : length of a BTO unit-cell), for which the quantum mechanical smearing²⁹ may be responsible. The estimations with $l_{\text{T-B}} - 1.5u_{\text{BTO}}$ were also tested. The effective thicknesses of the screening layer, i.e. the effective passive layer $l_{\text{I}}/2\epsilon_{\text{I}}$ of BTO/SrRuO₃ and BTO/Pt were estimated as 0.1 \AA and approximately 0.05 \AA , respectively²⁹.

Data availability

The data required to reproduce these findings can be provided upon reasonable requests to the corresponding author.

Received: 28 October 2020; Accepted: 1 January 2021

Published online: 25 January 2021

References

- Kittel, C. Physical theory of ferromagnetic domains. *Rev. Mod. Phys.* **21**, 541–583 (1949).
- Kalinin, S. V. & Bonnell, D. Domain polarity and temperature induced potential inversion on the BaTiO₃ (100) surface. *J. Appl. Phys.* **91**, 3816 (2002).
- Batra, I. P., Wurfel, P. & Silverman, B. D. Phase transition, stability, and depolarization field in ferroelectric thin films. *Phys. Rev. B* **8**, 3257–3265 (1973).
- Mehta, R. R., Silverman, B. D. & Jacobs, J. T. Depolarization fields in thin ferroelectric films. *J. Appl. Phys.* **44**, 3379–3385 (1973).
- Black, C. T., Farrell, C. & Licata, T. J. Suppression of ferroelectric polarization by an adjustable depolarization field. *Appl. Phys. Lett.* **71**, 2041–2043 (1997).
- Zhao, D. *et al.* Depolarization of multidomain ferroelectric materials. *Nat. Commun.* **10**, 2547–1–11 (2019).
- Tian, J. *et al.* Depolarization-field-induced retention loss in ferroelectric diodes. *Phys. Rev. Appl.* **11**, 024058–1–15 (2019).
- Kim, D. J. *et al.* Polarization relaxation induced by a depolarization field in ultrathin ferroelectric BaTiO₃ capacitors. *Phys. Rev. Lett.* **95**, 237602–1–4 (2005).
- Jo, J. Y., Kim, Y. S., Noh, T. W., Yoon, J.-G. & Song, T. K. Coercive fields in ultrathin BaTiO₃ capacitors. *Appl. Phys. Lett.* **89**, 232909–1–3 (2006).
- Schroeder, U., Lomenzo, P. D., Toriumi, A. & Mikolajick, T. Impact of depolarization fields on the ferroelectric switching behavior in doped HfO₂. *Ext. Abst. Fundament. Phys. Ferroelectr. Relat. Mater.* **2020**, 21–22 (2020).
- Polanco, M. A. M. *et al.* Stabilization of highly polarized PbTiO₃ nanoscale capacitors due to in-plane symmetry breaking at the interface. *Phys. Rev. B* **85**, 214107–1–7 (2012).
- Watanabe, Y. Proper permittivity for depolarization field in perfectly insulating ferroelectric and examination of background permittivity. *Ferroelectrics* **461**, 38–43 (2014).
- Watanabe, Y. Proper permittivity for depolarization field and its implication to universal instability of insulating ferroelectric: A note. *J. Phys. Soc. Jpn.* **79**, 034713–1–5 (2010) (Especially, Eqs. (4)–(10)).
- Watanabe, Y., Okano, M. & Masuda, A. Surface conduction on insulating BaTiO₃ crystal suggesting an intrinsic surface electron layer. *Phys. Rev. Lett.* **86**, 332–335 (2001).
- Watanabe, Y. Theoretical stability of the polarization in a thin semiconducting ferroelectric. *Phys. Rev. B* **57**, 789–804 (1998).
- Jiang, B. *et al.* Barium titanate at the nanoscale: Controlled synthesis and dielectric and ferroelectric properties. *Chem. Soc. Rev.* **48**, 1194–1228 (2019).
- You, W.-X. & Su, P. Depolarization field in ferroelectric nonvolatile memory considering minor loop operation. *IEEE Electron Device Lett.* **40**, 1415–1418 (2019).
- Watanabe, Y. Electrostatics liberating restrictions on ferroelectric by unification of polar discontinuity e^-h^+ layers and criteria of intrinsicity. *Ferroelectrics* **556**, 29–36 (2020).
- Watanabe, Y. Ferroelectricity of stress-free and strained pure SrTiO₃ revealed by ab initio calculations with hybrid and density functionals. *Phys. Rev. B* **99**, 064107–1–14 (2019).
- Kresse, G. & Hafner, J. Ab initio molecular dynamics for liquid metals. *Phys. Rev. B* **47**, 558R (1993).
- Kresse, G. & Joubert, D. From ultrasoft pseudopotentials to the projector augmented-wave method. *Phys. Rev. B* **59**, 1758 (1999).
- Kresse, G. & Furthmüller, J. Efficiency of ab-initio total energy calculations for metals and semiconductors using a plane-wave basis set. *J. Comput. Mater. Sci.* **6**, 15–50 (1996).
- Blöchl, P. E. Projector augmented-wave method. *Phys. Rev. B* **50**, 17953–17979 (1994).
- Monkhorst, H. J. & Pack, J. D. Special points for Brillouin-zone integrations. *Phys. Rev. B* **13**, 5188–5192 (1976).
- Perdew, J. P. *et al.* Restoring the density-gradient expansion for exchange in solids and surfaces. *Phys. Rev. Lett.* **100**, 136406–1–4 (2008).
- Resta, R. Macroscopic polarization in crystalline dielectrics: the geometric phase approach. *Rev. Mod. Phys.* **66**, 899–915 (1994).
- Perdew, J. P., Burke, K. & Ernzerhof, M. Generalized gradient approximation made simple. *Phys. Rev. Lett.* **77**, 3865–3868 (1996).
- Lichtenstein, A. I., Anisimov, V. I. & Zaanen, J. Density-functional theory and strong interactions: Orbital ordering in Mott-Hubbard insulators. *Phys. Rev. B* **52**, 5467R–5470R (1995).
- Watanabe, Y. Breakdown of ion-polarization-correspondence and born effective charges: Algebraic formulas of accurate polarization under field. *Phys. Rev. Mater.* **4**, 104405–1–11 (2020).
- Heine, V. Theory of surface states. *Phys. Rev. A* **138**, 1689–1696 (1965).
- Li, Y. L., Cross, L. E. & Chen, L. Q. A phenomenological thermodynamic potential for BaTiO₃ single crystals. *J. Appl. Phys.* **98**, 06410114 (2005) (For examples of standard GLD theories).
- Cross, L. E. & Pohanka, R. C. Ferroelectricity in bismuth oxide type layer structure compounds. *Mater. Res. Bull.* **6**, 939–949 (1971).
- Känzig, W. Ferroelectrics and antiferroelectrics. In *Solid State Physics* Vol. 4 (eds Seitz, E. & Turnbull, D.) 1–197 (Academic, New York, 1957).
- Haun, M. J., Furman, E., Jang, S. J., McKinstry, H. A. & Cross, L. E. Thermodynamic theory of PbTiO₃. *J. Appl. Phys.* **62**, 3331–3338 (1987).
- Tagantsev, A. K. Landau expansion for ferroelectrics: Which variable to use?. *Ferroelectrics* **375**, 19–27 (2008).
- Boni, G. A. *et al.* Low value for the static background dielectric constant in epitaxial PZT thin films. *Sci. Rep.* **9**, 14698 (2019).
- Watanabe, Y. Calculation of strained BaTiO₃ with different exchange correlation functionals examined with criterion by Ginzburg-Landau theory, uncovering expressions by crystallographic parameters. *J. Chem. Phys.* **148**, 194702 (2018).
- Garrity, K. F., Rabe, K. M. & Vanderbilt, D. Hyperferroelectrics: Proper ferroelectrics with persistent polarization. *Phys. Rev. Lett.* **112**, 27601–1–5 (2014).
- Liu, S. & Cohen, R. E. Stable charged antiparallel domain walls in hyperferroelectrics. *J. Phys. Condens. Matter* **29**, 244003 (2017).
- Krčmar, M. & Fu, C. L. Structural and electronic properties of BaTiO₃ slabs: Mechanism for surface conduction. *Phys. Rev. B* **68**, 115404–1–7 (2003).
- Sai, N., Fennie, C. J. & Demkov, A. A. Absence of critical thickness in an ultrathin improper ferroelectric film. *Phys. Rev. Lett.* **102**, 107601 (2009).
- Ji, D. *et al.* Freestanding crystalline oxide perovskites down to the monolayer limit. *Nature* **570**, 87–90 (2019).
- Ievlev, A. V. *et al.* Chemical state evolution in ferroelectric films during tip-induced polarization and electroresistive switching. *Appl. Mater. Interfaces* **8**, 29588–29593 (2016).
- Fong, D. D. *et al.* Stabilization of monodomain polarization in ultrathin PbTiO₃ films. *Phys. Rev. Lett.* **91**, 127601–1–4 (2006).

45. Deleuze, P.-M., Domenichini, B. & Dupont, C. Ferroelectric polarization switching induced from water adsorption in BaTiO₃ ultrathin films. *Phys. Rev. B* **101**, 075410 (2020).
46. Banieck, J. D. *et al.* Photoemission and quantum chemical study of SrTiO₃ (001) surfaces and their interaction with CO₂. *Phys. Rev. B* **78**, 195415-1–12 (2008).
47. De Souza, R. A., Metlenko, V., Park, D. & Weirich, T. E. Behavior of oxygen vacancies in single-crystal SrTiO₃: Equilibrium distribution and diffusion kinetics. *Phys. Rev. B* **85**, 174109-1–11 (2012) (**For example**).
48. Su, C.-P. *et al.* Impact of strain-field interference on the coexistence of electron and hole gases in SrTiO₃/LaAlO₃/SrTiO₃. *Phys. Rev. Mater.* **3**, 075003-1–10 (2019) (**For example**).
49. Hacene, M. *et al.* Accelerating VASP electronic structure calculations using graphic processing units. *J. Comput. Chem.* **33**, 2581–2589 (2012).
50. Hutchinson, M. & Widom, M. VASP on a GPU: Application to exact-exchange calculations of the stability of elemental boron. *Comput. Phys. Commun.* **7**, 1422–1426 (2011).
51. Momma, K. & Izumi, F. VESTA 3 for three-dimensional visualization of crystal, volumetric and morphology data. *J. Appl. Crystallogr.* **44**, 1272–1276 (2011).

Acknowledgements

Dr. P. Blöchel and Dr. M. Takashige for discussions, Dr. R. R. Mehta for his questions and discussions about Ref.¹³, and the support JSPS KAKENHI no. JP19K21853 are acknowledged.

Author contributions

Y.W. did this work.

Competing interests

The author declares no competing interests.

Additional information

Correspondence and requests for materials should be addressed to Y.W.

Reprints and permissions information is available at www.nature.com/reprints.

Publisher's note Springer Nature remains neutral with regard to jurisdictional claims in published maps and institutional affiliations.



Open Access This article is licensed under a Creative Commons Attribution 4.0 International License, which permits use, sharing, adaptation, distribution and reproduction in any medium or format, as long as you give appropriate credit to the original author(s) and the source, provide a link to the Creative Commons licence, and indicate if changes were made. The images or other third party material in this article are included in the article's Creative Commons licence, unless indicated otherwise in a credit line to the material. If material is not included in the article's Creative Commons licence and your intended use is not permitted by statutory regulation or exceeds the permitted use, you will need to obtain permission directly from the copyright holder. To view a copy of this licence, visit <http://creativecommons.org/licenses/by/4.0/>.

© The Author(s) 2021